PCCP

ARTICLE

Electronic Properties of Reduced Molybdenum Oxides

K. Inzani[a], M. Nematollahi[b], F. Vullum-Bruer[a], T. Grande[a], T. W. Reenaas[b] and S. M. Selbach[a]†

Received 00th January 20xx,
Accepted 00th January 20xx

DOI: 10.1039/x0xx00000x

www.rsc.org/

The electronic properties of MoO_3 and reduced molybdenum oxide phases are studied by density functional theory (DFT) alongside characterization of mixed phase MoO_x films. Molybdenum oxide is utilized in compositions ranging from MoO_3 to MoO_2 with several intermediary phases. With increasing degree of reduction, the lattice collapses and the layered MoO_3 structure is lost. This affects the electronic and optical properties, which range from the wide band gap semiconductor MoO_3 to metallic MoO_2. DFT is used to determine the stability of the most relevant molybdenum oxide phases, in comparison to oxygen vacancies in the layered MoO_3 lattice. The non-layered phases are more stable than the layered MoO_3 structure for all oxygen stoichiometries of MoO_x studied where $2 \leq x < 3$. Reduction and lattice collapse leads to strong changes in the electronic density of states, especially the filling of the Mo 4*d* states. The DFT predictions are compared to experimental studies of molybdenum oxide films within the same range of oxygen stoichiometry. We find that whilst MoO_2 is easily distinguished from MoO_3, intermediate phases and phases mixtures have similar electronic structures. The effect of the differing band structures is seen in the electrical conductivity and optical transmittance of the films. Insight into the oxide phase stability ranges and mixtures is not only important for understanding molybdenum oxide films for optoelectronic applications, but is also relevant to other transition metal oxides such as WO_3 which exist in analogous forms.

1 Introduction

In order to utilize molybdenum oxide films, it is important to understand how optical and electrical properties change with stoichiometry and crystal structure. Molybdenum oxide has applications in numerous optical and electronic devices, including organic light emitting diodes, photodetectors, gas sensors, photovoltaics, batteries and multi-chromic coatings.[1–9] The layered structure of MoO_3 has proved useful in creating many highly oriented nanostructures, such as two-dimensional flakes and belts, as well as nanorods, nanowires and nanoparticles.[3,10–18] These architectures are often seen in the morphology of thin films, where they can be exploited for their novel properties.[14,16–24] For such wide-ranging applications, there exist many combinations of stoichiometry, crystallinity and morphology.[6,25–29] In addition, phase mixtures of compositions MoO_x for $2 < x < 3$ can be present in films and devices.[30–34] Many reported devices rely on sub-stoichiometric MoO_3, with mid-gap states necessary for device operation.[1,26,27,31,33,35–38] However it is unlikely that oxygen vacancies remain as point defects, as ordering of oxygen vacancies has been observed at very low concentrations.[39]

The crystal structures of molybdenum oxide phases can be spilt into three groups: those based on the layered MoO_3 structure, those based on the distorted ReO_3 structure, and MoO_2 which exists in the distorted rutile structure. The stable, orthorhombic polymorph of MoO_3 is built up of distorted MoO_6 octahedra which are edge and corner sharing in two directions, forming bilayers which are held together by dispersed interactions. The separation of the layers is known as the van der Waals gap. There are oxygen ions on three symmetrically inequivalent positions – O1, singly coordinated and pointing towards the van der Waals gap, O2, corner-sharing and O3, edge-sharing. Metastable structures based on crystallographic shear of MoO_3 have been observed in the reduction of MoO_3.[40-43] These fall into the series Mo_nO_{3n-m+1}, in which only $Mo_{18}O_{52}$ has been produced in pure form.[44] Upon further reduction, the lattice collapses into ReO_3 type structures with crystallographic shear planes. These are described by the Magnéli series Mo_nO_{3n-1}, for which Mo_9O_{26} and Mo_8O_{23} are known to exist.[45,46] Early calculations based on a cluster model found that oxygen vacancy formation is more favourable when accompanied by crystallographic shear, in both molybdenum oxide and rhenium oxides.[47] In addition, the $Mo_{17}O_{47}$ and Mo_5O_{14} phases are based on pentagonal bipyramids within the ReO_3 structure.[48,49] Mo_4O_{11}, most stable in the orthorhombic form, can also be described by the ordered emission of oxygen from the ReO_3 lattice.[49,50] In this work, the ReO_3 based structures are described as non-layered due to the loss of the van der Waals gap. A recent study has been done to develop a thermodynamic description of the Mo-O system using the CALPHAD (CALculation of PHAse Diagrams) method.[51] To complete the phase diagram, a lack of reliable

[a] Department of Materials Science and Engineering, NTNU Norwegian University of Science and Technology, N-7491 Trondheim, Norway.
[b] Department of Physics, NTNU Norwegian University of Science and Technology, N-7491 Trondheim, Norway.
† Phone: +47-73-59-40-99; e-mail: selbach@ntnu.no.
DOI: 10.1039/x0xx00000x

thermochemistry data prompted the use of first principles density functional theory (DFT) calculations.

The electronic structure of MoO_3 has been modelled by Scanlon *et al.* in good agreement with X-ray photoemission spectra.[52] MoO_3 is a semiconductor with a band gap of 3.2 eV in a thin film.[11,53] Other studies have investigated the electronic details of oxygen vacancies in MoO_3, such as the localisation of electrons on surface vacancies.[54,55] Electrons donated from oxygen vacancies fill Mo 4*d* states which then lie in the band gap as gap states.[54,56] The stabilization of shear structures of oxygen deficient MoO_3 and ReO_3 has been ascribed to filling of Mo 4*d* states in the formation of Mo-Mo bonds.[47] Thus, oxygen vacancies provide n-type doping which enables alignment of band levels with metals, oxides and organic molecules, via band bending and charge transfer doping.[36,56] The high work function of MoO_3 means that its role in organic electronic devices is as a hole conductor, despite its n-type nature.[36] Distortion of the MoO_3 lattice and electron doping has been shown to reduce the band gap.[57] Furthermore, amorphous MoO_x films have exhibited a metallic band structure, due to states at the Fermi level attributed to Mo^{4+} ions.[37] A transition to correlated metal conduction was demonstrated for MoO_x close to x = 2.6, although the lattice structure was not determined.[28] It is known that MoO_2 is metallic based on the Mo-Mo bonding in the distorted rutile structure, and Scanlon *et al.* found that the Fermi energy lies in a trough in the density of states.[52,58] Although Mo_4O_{11} is the next most stable oxide phase, it has not been extensively studied with respect to electronic structure, but is predicted to be metallic.[10]

In order to elucidate the structure-property relations of the reduced molybdenum oxides, we use density functional theory to predict the electronic structure of a representative sample of MoO_3 and ReO_3 lattice types. We find the stabilities relative to MoO_2 and MoO_3, and include a comparison with oxygen vacancies as point defects in various concentrations. The theoretical predictions are compared to X-ray photoelectron spectra and measured optical properties of molybdenum oxide films with a range of oxygen stoichiometries.

2 Methods

Computational details

DFT calculations were performed using the Vienna Ab initio Simulation Package (VASP) with the projector augmented wave (PAW) pseudopotentials Mo_sv ($4s^2 4p^6 5s^1 4d^5$) and O_h ($2s^2 2p^4$) supplied with VASP.[59–62] Based on previous testing of exchange functionals used with vdW-DF, the functional vdW-DF2 was used for optimization of MoO_3.[63] The DFT + U approach of Dudarev *et al.* was applied to the Mo 4*d* to better match the lattice parameters and band structures.[64] A U correction of 5 eV was used, based on the value previously determined by comparison of the position of band gap states with experimental results.[63] Supercells of MoO_3 were used to replicate three different finite concentrations of oxygen vacancies. Cell sizes 1x1x1, 2x1x2 and 3x1x3 were each used with a single oxygen vacancy, corresponding to O/Mo ratios of 2.75, 2.9375 and 2.972 respectively. The calculations were repeated for vacancies on each of the three oxygen lattice positions.

Structural optimization was also done on selected molybdenum oxide phases. The most experimentally stable structure from each of the series and structure types was chosen, thus the oxides examined were $Mo_{18}O_{52}$, monoclinic Mo_9O_{26}, $Mo_{17}O_{47}$, orthorhombic Mo_4O_{11} and MoO_2. The vdW-DF approach did not perform well with the non-layered structures. Instead, GGA, PBEsol and LDA were tested for optimization of these structures (Table 1). GGA predicted larger and LDA predicted smaller lattice parameters than experimental values, whilst the PBEsol functional gave values in between. This is in agreement with calculations in another study of the Mo-O system which found PBEsol to give excellent agreement with experiment.[51] In addition, the MoO_3 structure was optimized with PBEsol in order to compute relative enthalpies. A U value of 5 eV was applied to Mo 4*d* in keeping with the treatment of electron correlation in MoO_3. However, electron correlation is known to vary with oxidation state and the best choice of U will not be the same for MoO_2. To overcome this for electronic structure calculations, a non-self-consistent calculation with the hybrid functional HSEsol was done to determine the density of states after pre-convergence of eigenvalues with PBEsol.[65]

Convergence was reached for an energy cut-off for the plane-wave basis set of 810 eV. For a unit cell of MoO_3 a 6x2x6 Gamma centered k-point grid was used for Brillouin zone integration, with equivalent k-point density used for other unit cells. All considered structures were fully optimized until the residual forces on the ions were less than 0.05 eV·Å^{-1}. For the hybrid calculations, an energy cut-off of 400 eV was used with (PAW) pseudopotentials Mo_sv and standard O.[59–62] For metallic structures the Methfessel Paxton sampling scheme was used, in which case the contribution of the electronic entropy was less than 0.1 meV·atom^{-1} and considered negligible. The zero-point energy was not taken into account.

Experimental details

Films of molybdenum oxide were synthesised by pulsed laser deposition. A KrF excimer laser (Lambda Physics COMPex Pro 110, 248 nm, 20 ns) was operated at 10 Hz to ablate a MoO_3 target (Testbourne Ltd., 99.95% pure). Before each deposition, the target was pre-ablated by 3000 pulses to regulate the target condition. The films were deposited on Si (100) and quartz substrates which were prepared by degreasing with ethanol and acetone. The target to substrate distance was 4 cm for all films, and 18,000 pulses were used for the depositions. Deposition temperatures were 500 and 570 °C. The chamber base pressure was $\leq 1.3\times10^{-5}$ Pa with O_2 gas flow in the range of 55 to 70 sccm, resulting in a corresponding background pressure of 2.4 and 4.5 Pa, respectively. The films are denoted by their deposition conditions [°C]/[Pa]: 500/4.5, 500/2.4 and 570/2.4. These had the corresponding growth rates 2.97, 2.17 and 0.94 Å sec^{-1}.

Table 1 Reference experimental lattice parameters and calculated lattice parameters for MoO_2, MoO_3 and $Mo_{18}O_{52}$, calculated with GGA, LDA, PBEsol and vdW-DF2, with U = 0 or 5 eV. Percentage deviation from experimental values is given in brackets below

		U (eV)	a (Å) (Δ (%))	b (Å) (Δ (%))	c (Å) (Δ (%))	α (°) (Δ (%))	ß (°) (Δ (%))	γ (°) (Δ (%))
MoO_2	Experimental [66]		5.537	4.859	5.607		119.37	
	GGA	0	5.594 (1.0)	4.890 (0.6)	5.654 (0.8)		120.86 (1.2)	
	LDA	0	5.506 (-0.6)	4.826 (-0.7)	5.555 (-0.9)		120.86 (1.2)	
	PBEsol	0	5.513 (-0.4)	4.842 (-0.4)	5.563 (-0.8)		120.89 (1.3)	
	PBEsol	5	5.515 (-0.4)	4.914 (1.1)	5.591 (-0.3)		121.22 (1.5)	
	vdW-DF2	0	5.738 (3.6)	4.957 (2.0)	5.748 (2.5)		121.14 (1.5)	
	vdW-DF2	5	5.769 (4.2)	5.022 (3.4)	5.814 (3.7)		121.60 (1.9)	
MoO_3	Experimental [67]		3.963	13.855	3.696			
	GGA	0	3.927 (-0.9)	14.191 (2.4)	3.687 (-0.2)			
	LDA	0	3.799 (-4.1)	13.005 (-6.1)	3.669 (-0.7)			
	PBEsol	0	3.852 (-2.8)	13.556 (-2.2)	3.677 (-0.5)			
	PBEsol	5	3.809 (-3.9)	13.490 (-2.6)	3.735 (1.1)			
	vdW-DF2	0	3.976 (0.3)	13.876 (0.1)	3.743 (1.3)			
	vdW-DF2	5	3.914 (-1.2)	13.900 (0.3)	3.801 (2.8)			
$Mo_{18}O_{52}$	Experimental [44]		8.15	11.89	21.23	102.67	67.82	109.97
	vdW-DF2	5	8.191 (0.6)	12.108 (1.8)	21.435 (1.0)	102.61 (-0.1)	67.91 (0.1)	109.71 (-0.2)
	PBEsol	5	8.031 (-1.4)	11.890 (0.0)	20.912 (-1.5)	102.67 (0.0)	67.80 (0.0)	109.68 (-0.3)

Determination of the phase composition of the films was done by X-ray diffraction (XRD) using a Bruker AXS D8 Focus with Solid state LynxEye™ detector. CuKα radiation source was used in Bragg-Bretano geometry (0.01° step size, 1.5 s step time and 10° to 60° 2θ). XRD was carried out on films on Si substrates in order to eliminate the amorphous background of quartz substrates. Scanning electron microscopy (SEM, Hitachi S-5500, 30 kV) was performed on film cross-sections to investigate film thickness and morphology. The root mean square roughness of film surfaces was determined by atomic force microscopy (AFM, Veeco Multimode V, Nanoscope software) with Peak Force Tapping™ in ScanAsyst mode over a 1 µm x 1 µm area.

X-ray photoelectron spectroscopy (XPS) was used to determine the oxidation states present and their relative content was used to infer the oxygen stoichiometry. This was obtained with a Kratos Axis Ultra with monochromatic Al Kα X-ray source (hv = 1486.6 eV, 15 mA, 15 kV, with lowest energy resolution 150 meV). The binding energies (Eb) were corrected by Eb equal to 284.8 eV of adventitious C1s. XPS survey scans were performed within 2 min for surface elemental analysis. The Mo 3*p* and Mo 3*d* core levels were measured for the Eb range 385–427 eV and 219–242 eV, respectively. Measurements were carried out with a pass energy of 20 eV. Background modelling and subtraction, peak fitting and quantification of the components were processed using CasaXPS software (version 2.3.16). Prior to peak fitting, an offset Shirley background was subtracted from the spectrum. The offset Shirley background was calculated from a blend of a Shirley and linear backgrounds $OS(E{:}\lambda) = S(E)(1-\lambda) + L(E)\lambda$, where the Shirley and the linear background are represented by $\lambda = 0$, and $\lambda = 1$, respectively. In the curve fitting models, $\lambda = 0.3$ is used for all the components. Mo 3*p* and Mo 3*d* peaks were symmetrical and a Lorentzian line shape was used. A Gaussian is also convoluted to consider the Gaussian instrumental broadening in addition to the Lorentzian energy distribution of the electrons.

The sheet resistivity of the films was determined using a Singatone four point probe and a Keithley 2449 5A SourceMeter for films on quartz substrates. The radius of the tips was 0.125 mm and the spacing between them 1 mm. A UV/Vis/NIR spectrophotometer (OLIS 14) was used to measure the transmittance of the films over the range 250 – 2100 nm.

3 Results and discussion

Density functional theory calculations

Oxygen vacancies in layered MoO_3. The layered structure of orthorhombic MoO_3 is well described by the exchange functional with vdW-DF, vdW-DF2, as discussed in a previous study considering the dilute limit of oxygen vacancies in MoO_3.[63] Here, finite concentrations of oxygen vacancies are considered. Oxygen vacancies on the O1, O2 and O3 positions were modelled individually inside three supercells, (1x1x1 = 16 atoms, 2x1x2 = 64 atoms, 3x1x3 = 144 atoms) and the ion positions and cell volume were allowed to relax. These correspond to stoichiometries of $MoO_{2.75}$, $MoO_{2.9375}$ and $MoO_{2.972}$ respectively. The ground state lattice parameters and MoO_3 unit cell volumes with supercell size are shown in Figure 1. As expected, the perfect structure shows negligible change with supercell size, within 0.01 Å of atomic positions. In the case of the 1x1x1 cell, the vacancies have a large effect on different cell parameters. The O1 vacancy yields a smaller *a* parameter whilst increasing *c,* with relatively unchanged *b* parameter across the van der Waals gap. The O2 vacancy gives the same trends but with smaller deviation from the stoichiometric lattice. The O3 vacancy, however, shows a large increase in *b* with decreased *a* and *c*. These contributions result in a similar unit cell volume for all three vacancies, which is smaller than the stoichiometric volume by 1.2-1.3 Å^3. The large effect on the 1x1x1

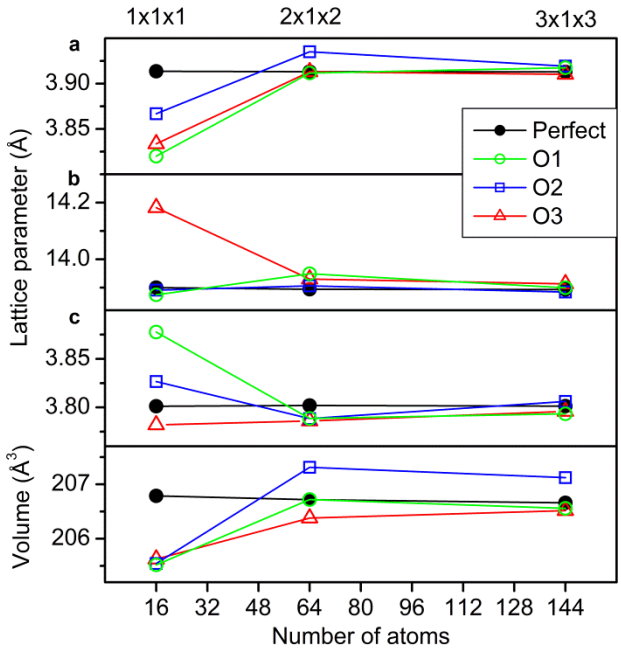

Figure 1 Lattice parameters and unit cell volume of MoO_3 supercells with vacancies on O1, O2 and O3 positions.

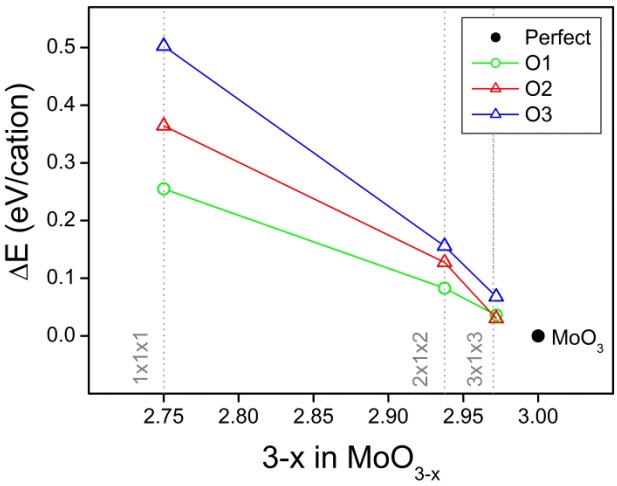

Figure 2 Energy difference per cation versus stoichiometry, for MoO_3 supercells with vacancies on O1, O2 and O3 positions, compared to stoichiometric MoO_3. Values are corrected for mass balance by the chemical potential of oxygen in the MoO_3-MoO_2 regime.

cell is a result of the high vacancy concentration, and with a lower vacancy concentration there are lesser effects on the lattice cell parameters. The 2x1x2 cell has lattice parameters converged within 0.05 Å and the 3x1x3 cell within 0.02 Å with respect to the stoichiometric structure. The volume changes are within 0.6 Å^3 and 0.5 Å^3 for the 2x1x2 and 3x1x3 cells respectively. This shows that the larger cell size effectively screens the elastic interactions between the point defects.

The energy cost of oxygen vacancies decreases with decreasing vacancy concentration, approaching the stoichiometric composition. The energy difference per MoO_3 formula unit with the three vacancy concentrations is given in Figure 2. For all concentrations, the O1 vacancy has lowest energy difference, except the 3x1x3 cell where the O2 vacancy position is equivalent to O1 within 6 meV. It can be expected that the O1 vacancy position is the most energetically favourable as it breaks only one Mo–O bond. This is in agreement with a previous theoretical study of surface oxygen vacancies in MoO_3.[55]

Locally, the charge compensating electrons act to distort the vacancy containing octahedra. The bond lengths of the octahedron containing the O1 vacancy in the three supercells are shown in Figure 3. In the 1x1x1 case, the Mo ion is shifted away from the vacancy and displaced in the direction of the asymmetrically bridging, corner-sharing oxygens, shortening four out of five of the bonds. Baur's distortion index[68] is decreased in this case, from 0.093 for the stoichiometric octahedron to 0.024 for the square pyramid of the O1 vacancy in the 1x1x1 cell. This is reflected in the density of states, shown in Figure 4, in which there is smearing of the filled Mo 4*d* states across the entire band gap, to the extent that the DOS is metallic. The 2x1x2 and 3x1x3 cells exhibit a different distortion in which the Mo ion is shifted towards the vacancy. This allows an overall lengthening of the bonds in order to accommodate the charge compensating electrons. There is an increase in the distortion indices to 0.139 for both the 2x1x2 and 3x1x3 supercells. The DOS shows a narrow band of Mo 4*d*

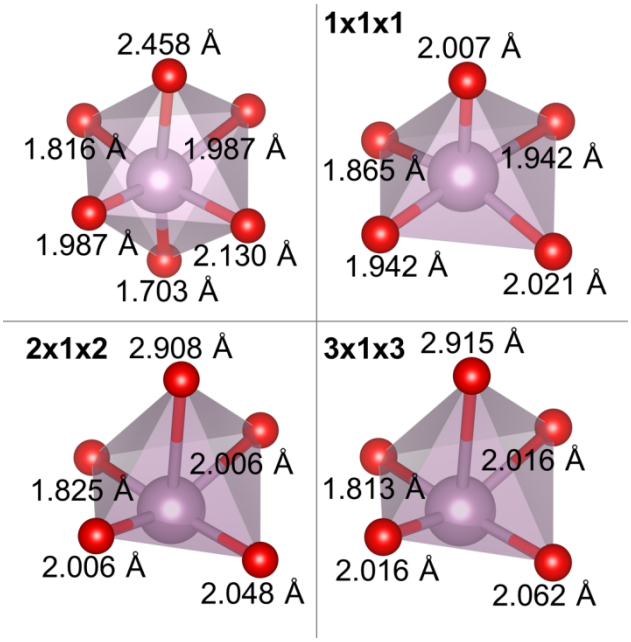

Figure 3 Mo–O bond lengths of an octahedron in stoichiometric MoO_3, and the bond lengths of distorted polyhedrons adjacent to an apical O1 vacancy in 1x1x1, 2x1x2 and 3x1x3 supercells.

states within the band gap. Compared to the calculated band gap of the perfect structure, 1.56 eV, the 3x1x3 and 2x1x2 supercells with an O1 vacancy have band gaps of 1.50 and 1.32 eV, respectively. The reduced band gap of the 2x1x2 supercell is due to the higher dispersion with the increase in concentration of charge compensating electrons. The similarity in the octahedral distortion and DOSes between the vacancies in 2x1x2 and 3x1x3 supercells further demonstrates that the point defect interaction is already well screened in the 2x1x2 supercell.

Reduced molybdenum oxides. MoO_3 and the reduced molybdenum oxide phases are compared by using the PBEsol functional. The lattice parameters given by the PBEsol functional are given in Table 2, and the crystal structures and unit cells are shown in Figure 5. As the dispersed interactions of the layered MoO_3 and $Mo_{18}O_{52}$ structure are not well described by PBEsol, there is a larger deviation from the experimental lattice parameters than with vdW-DF2 (Table 1), and the lattice parameters across the van der Waals gap are underestimated. There is reasonable agreement in the lattice parameters of Mo_9O_{26} and $Mo_{17}O_{47}$. The deviations may also stem from the uncertainty in experimental determination of these structures.[44,45,48] Mo_4O_{11} and MoO_2 are better matched, within -1.2 Å of experimental parameters.

The enthalpy of formation for the four intermediate Mo-O phases and three finite O1 vacancy concentrations relative to MoO_2 and MoO_3 was calculated at T = 0 K by the relation,

$$\Delta H = E0(MoO_{3-x}) - E0(MoO_3) + x\cdot(E0(MoO_3) - E0(MoO_2))$$

where E0 is the ground state energy given by DFT, which provides an approximation to the energy of the closed isothermal and isobaric system. ΔH per cation is shown with oxygen stoichiometry in Figure 6, in which the solid line indicates the convex hull formed by the most stable DFT

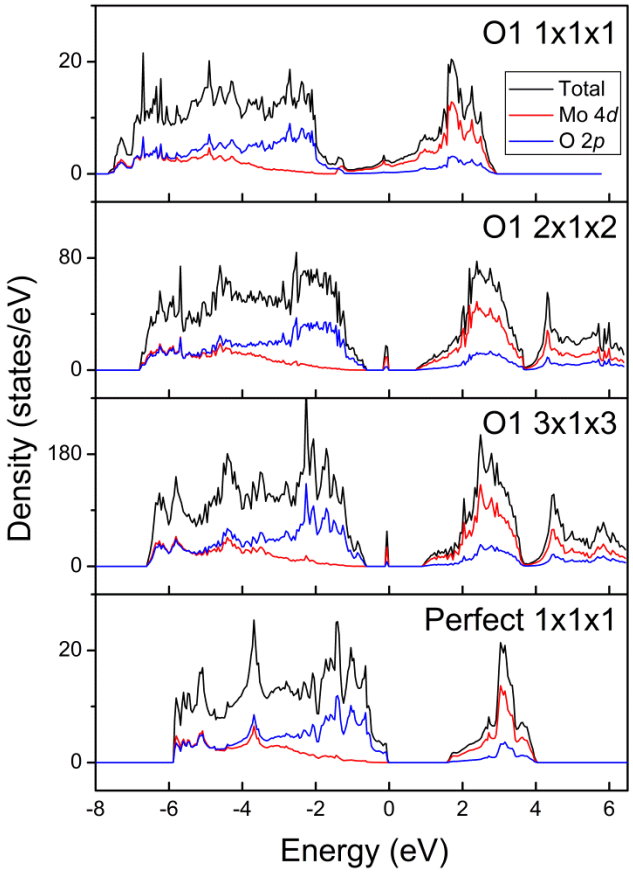

Figure 4 Total and orbital resolved density of states for an O1 vacancy in 1x1x1, 2x1x2 and 3x1x3 supercells, compared to a perfect lattice. The Fermi energy is set at 0 eV.

ground state structures for a given stoichiometry.[70] The convex hull connects the phases that are stable against decomposition into the other phases, and consists of MoO_2, $Mo_{17}O_{47}$, Mo_9O_{26} and MoO_3. Any phase lying above the convex hull but with negative ΔH is favourable to form from the primary oxides, but is thermodynamically unfavourable relative to the ground state. All intermediate phases have a negative ΔH, which means that they are stable relative to the end phases. For the two stoichiometrically equivalent phases Mo_9O_{26} and $Mo_{18}O_{52}$, Mo_9O_{26} is a vertex of the convex hull whereas $Mo_{18}O_{52}$ lies 220 meV above it. Thus, the non-layered Mo_9O_{26} was calculated to be more thermodynamically stable than the layered $Mo_{18}O_{52}$. Mo_4O_{11} lies above the convex plot, 108 meV higher than the similarly reduced $Mo_{17}O_{47}$. This result is contrary to experimentally determined phase diagrams, from which Mo_4O_{11} is known to be the most stable intermediate phase.[51,71] This discrepancy can be related to the difference in comparing 0 K ground state structures to finite temperature experimental data, and effects of entropy as well as errors innate to the DFT method can be considered. Firstly, there is a lack of data on the low temperature stabilities of molybdenum oxides. The thermodynamics-based CALPHAD method has provided data which is well matched to experimental data, suggesting that thermodynamic considerations are at least partly at fault, however, it was noted that the compositional homogeneity range of the intermediate oxide phases is small, suggesting that configurational entropy may not play a large

role.[51] Alternatively, DFT could be used to evaluate the true ground state at finite temperatures by calculation of phonon spectra, which would indicate the effect of vibrational entropy. In contrast to the CALPHAD data, DFT calculations of formation enthalpies were shown to be strongly dependent on method. In particular, the choice of U value may be a source of discrepancy amongst the various phases, as the electron correlation varies across the reduction degree as well as with crystal structure. The difference in formation enthalpy between Mo_4O_{11} and $Mo_{17}O_{47}$ is a similar magnitude to that of two polymorphs of MoO_3 where the discrepancy of DFT calculated relative stability with experimental data was attributed to a U value that could not adequately describe both phases.[51] However, it is hard to quantify the error from these DFT calculations as, to our knowledge, there is no experimental data available on the formation enthalpy of $Mo_{17}O_{47}$.

The three O1 vacancy concentrations each have a positive ΔH. This suggests that the intermediate phases are energetically favourable compared to any finite concentration of oxygen vacancies in MoO_3. This corroborates with previous observations that vacancy ordering occurs at very low oxygen vacancy concentrations.[72] The oxygen vacancies which distort the lattice come at an energy cost, and non-stoichiometry is better accommodated by annihilation of vacant anion sites by crystallographic shear planes. Furthermore, it is believed that the oxomolybdenum cations, $(Mo{=}O)^{4+}$, stabilize the layered structure of MoO_3.[73] It follows that the sheared $Mo_{18}O_{52}$ structure, which no longer has one $(Mo{=}O)^{4+}$ bond per cation, is destabilized relative to the non-layered structure of Mo_9O_{26}. This could also be a reason why all known phases with a smaller O/Mo ratio are non-layered, i.e. they do not exhibit a van der Waals gap.

MoO_3, Mo_9O_{26}, Mo_4O_{11} and MoO_2 are the most studied molybdenum oxides, and their density of states are shown in Figure 7. The HSEsol functional gives an improved treatment of unoccupied bands compared to the DFT+ U method. The band gap of MoO_3 is calculated as 2.84 eV, which is within the range of experimentally determined values of 2.7-3.4 eV.[31,53] The valence band is composed mainly of O 2*p* states, and the width increases from MoO_3 to Mo_9O_{26} and Mo_4O_{11} as there is smearing of O 2*p* states into the band gap. The other effect of decreasing O/Mo ratio is that Mo 4*d* states are filled and lowered in energy, narrowing the band gap, and the Fermi level therefore lies in the conduction band. This results in a metallic character of Mo_9O_{26}, Mo_4O_{11} and MoO_2. This differs from the gap states in the DOS of oxygen vacancies in MoO_3, in which the Mo 4*d* states are separated from the conduction band, due to the filling of Mo 4*d* states by charge compensating electrons. In the non-layered structures however, the Mo 4*d* states are filled due to the formation of Mo–Mo bonds, which are not strong enough to split the band off from the rest of the unoccupied conduction band. MoO_2 has a higher density of occupied Mo 4*d* states per cation, characterized by two narrow peaks. The higher intensity of these peaks is attributed to the Mo–Mo bonding which is present for every cation in MoO_2, but is confined to fewer cations in the Mo_4O_{11} and Mo_9O_{26} structures (Figure 5). This corroborates with conductivity measurements, which show the metallic nature MoO_2 and increased resistivity in Mo_4O_{11} and Mo_9O_{26}.[46,69,74]

Table 2 Calculated lattice parameters for molybdenum oxides calculated with PBEsol and U = 5 eV, with percentage deviation from experimental values, and reference experimental lattice parameters given in brackets.

	a (Å)	Δ (%)	b (Å)	Δ (%)	c (Å)	Δ (%)	α (°)	Δ (%)	ß (°)	Δ (%)	γ (°)	Δ (%)	Ref.
MoO_3	3.809	-3.9	13.490	-2.6	3.735	1.1							
	(3.963)		(13.855)		(3.696)								67
$Mo_{18}O_{52}$	8.031	-1.4	11.890	0.0	20.912	-1.5	102.67	0.0	67.80	0.0	109.68	-0.3	
	(8.15)		(11.89)		(21.23)		(102.67)		(67.82)		(109.97)		44
Mo_9O_{26}	17.015	1.6	3.861	-3.9	14.750	1.5			94.98	-0.8			
	(16.74)		(4.019)		(14.53)				(95.75)				45
$Mo_{17}O_{47}$	21.928	1.4	19.776	0.7	3.775	-4.5							
	(21.615)		(19.632)		(3.952)								69
Mo_4O_{11}	24.397	0.0	6.675	-0.7	5.385	-1.2							
	(24.40)		(6.723)		(5.45)								50
MoO_2	5.515	-0.4	4.914	1.1	5.591	-0.3			121.22	1.5			
	(5.537)		(4.859)		(5.607)				(119.37)				66

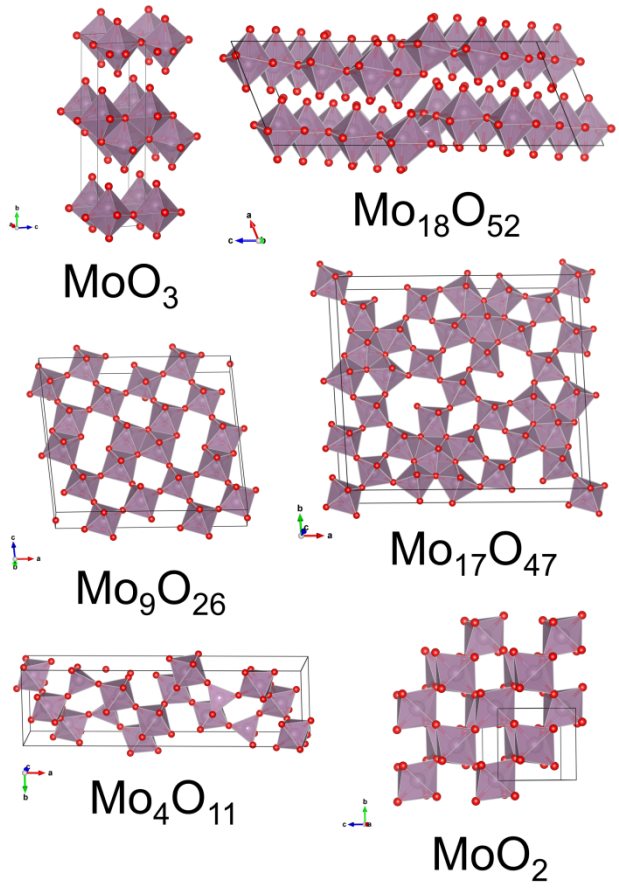

Figure 5 The crystal structures of the modelled molybdenum oxides, with their respective single unit cells shown.

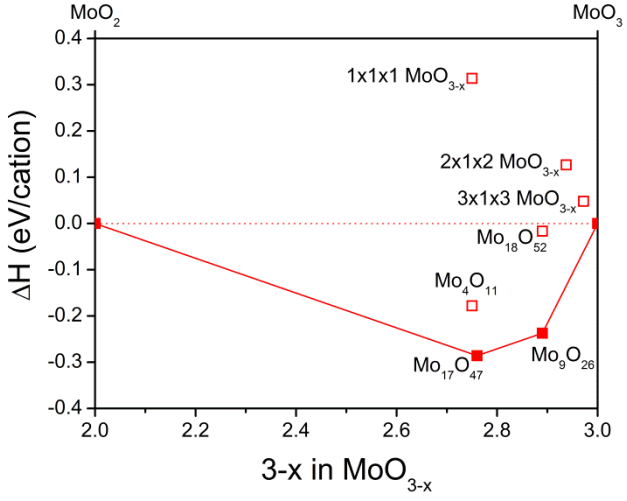

Figure 6 Enthalpy of formation (ΔH) relative to the end members MoO_3 and MoO_2, for four Mo-O phases and three finite oxygen vacancy concentrations in MoO_3. The solid line represents the convex hull which connects the phases that are most thermodynamically stable against decomposition into other phases or the end members.

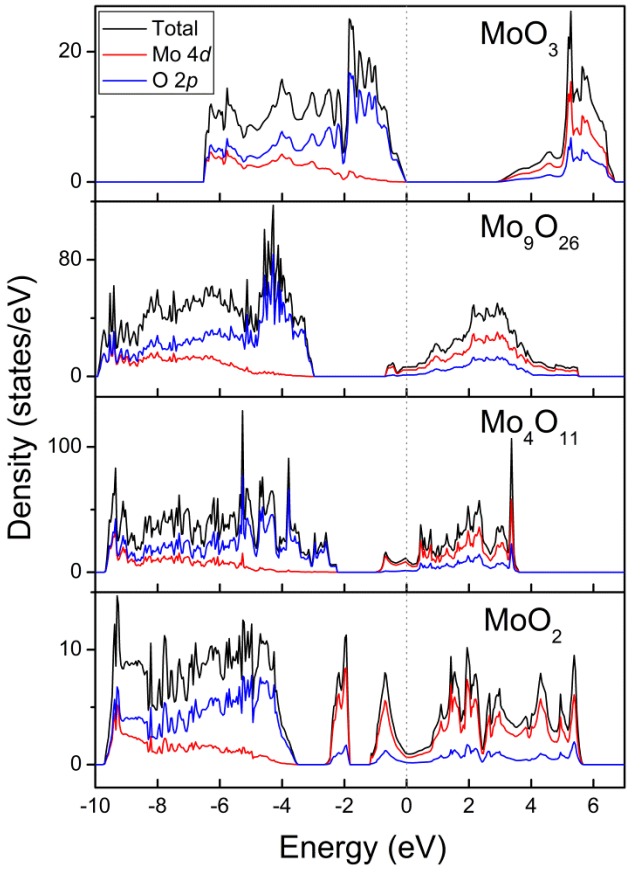

Figure 7 Total and orbital resolved density of states of molybdenum oxides MoO_3, Mo_9O_{26}, Mo_4O_{11} and MoO_2. DOSes were calculated in a non-self-consistent electronic calculation with HSEsol, from eigenvalues pre-converged with PBEsol. The DOSes are aligned with the Fermi energy set to 0 eV.

Structure and properties of thin films

The deposition parameters of temperature and oxygen partial pressure affect the composition of the film by creating more reducing or more oxidising conditions. The lower temperature of 500 °C and higher pressure of 4.5 Pa allows orthorhombic MoO_3 to form. This is shown in the XRD pattern of 500/4.5 in Figure 8, which matches the MoO_3 reference pattern, but also shows some reflections of the Mo_4O_{11} phase. For a lower deposition pressure, the 500/2.4 film has reflections of Mo_4O_{11} and MoO_2. The most reduced is the 570/2.4 film, which shows strong MoO_2 reflections and faint reflections of Mo_4O_{11}. In addition, the 500/4.5 and 570/2.4 films exhibit a broad reflection at low values of 2θ, whereas the 500/2.4 film does not. This broad reflection can indicate the presence of an amorphous phase.

The morphology of the films differs with deposition conditions, as evident from cross-sections of the three deposited films in the SEM micrographs in Figure 9. The 500/4.5 film consists of columnar grains in a dense, forest-like structure. Film 500/2.4 consists of highly oriented rods. There is an apparent difference in crystallinity between these films that can explain the amorphous background of the more oxidized film. The sharp peaks of the Mo_4O_{11} phase in the XRD pattern suggest that the highly crystalline rods are Mo_4O_{11}. In

addition, there is a dense layer adjacent to the substrate, approximately one third of the thickness of the entire film. This has a similar morphology to the 570/2.4 film, so the MoO_2 content is likely confined to the bottom third of the 500/2.4 film. The 570/2.4 film is considerably thinner and less oriented, and appears to have an overall higher density. This is reflected in the RMS roughness values which is lowest for the 570/2.4 film. The film thicknesses and RMS roughness are given in Table 3, as well as the measured resistivity. The sheet resistivity, $\rho_{\square}$, was calculated by $\rho_{\square} = \frac{\pi}{\ln(2)}\frac{V}{I}$

and the bulk resistivity, ρ, by $\rho = t\frac{\pi}{\ln(2)}\frac{V}{I}$

where V is the voltage, I is the current and t is the film thickness. The 500/4.5 film had a high resistivity that could not be measured with our experimental setup. The resistivity measurements are consistent with the calculated band

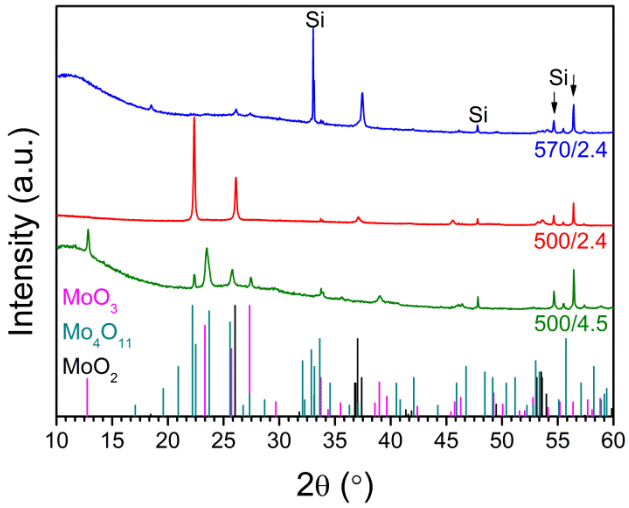

Figure 8 XRD patterns of the molybdenum oxide films, with the reference diffraction patterns MoO_3 (PDF 00-005-0508), Mo_4O_{11} (PDF 00-005-0337) and MoO_2 (00-032-0671). Reflections from the silicon substrate are labelled with Si.

Table 3 Film properties: root mean square roughness, Rq, measured over a 1 um x 1 um area; thickness measured by SEM cross-section; sheet resistivity, $\rho_{\square}$, and bulk resistivity ρ.

[T]/[P] (°C)/(Pa)	Rq (nm)	Thickness (nm)	$\rho_{\square}$ ($\Omega\square^{-1}$)	ρ (Ω·cm)
500/4.5	25.9	570 ± 80 nm	-	-
500/2.4	37.5	400 ± 40 nm	227.2	9.09×10^{-3}
570/2.4	13.1	175 ± 25 nm	949.9	16.62×10^{-3}

structure, showing the metallic nature of Mo_4O_{11} and MoO_2, and insulating nature of MoO_3. Resistivity depends strongly on stoichiometry, and these results are close to values reported for films with stoichiometry $MoO_{2.3}$.[28] Furthermore, the morphology of the 500/4.5 film is rod-like throughout, which will also impact the conductivity severely. The 500/2.4 and 570/2.4 films have a continuous layer, facilitating the carrier transport. The lower resistivity of the 500/2.4 film compared to the 570/2.4 film could be due to the high crystallinity seen by SEM.

The composition and stoichiometry of the films can be further elucidated by XPS analysis. Deconvolution of the spectra is displayed in Figure 10, with fitting parameters given in Table 4. The phase segregation and difference in crystallinity between phases that is clearly seen in the microstructure of the films influences both the XRD and XPS results. Knowledge of this morphology allows a consistent interpretation of both techniques. The 500/4.5 film mainly contains Mo^{6+}, with 14 % Mo^{5+}. This corresponds to the XRD analysis that the film is

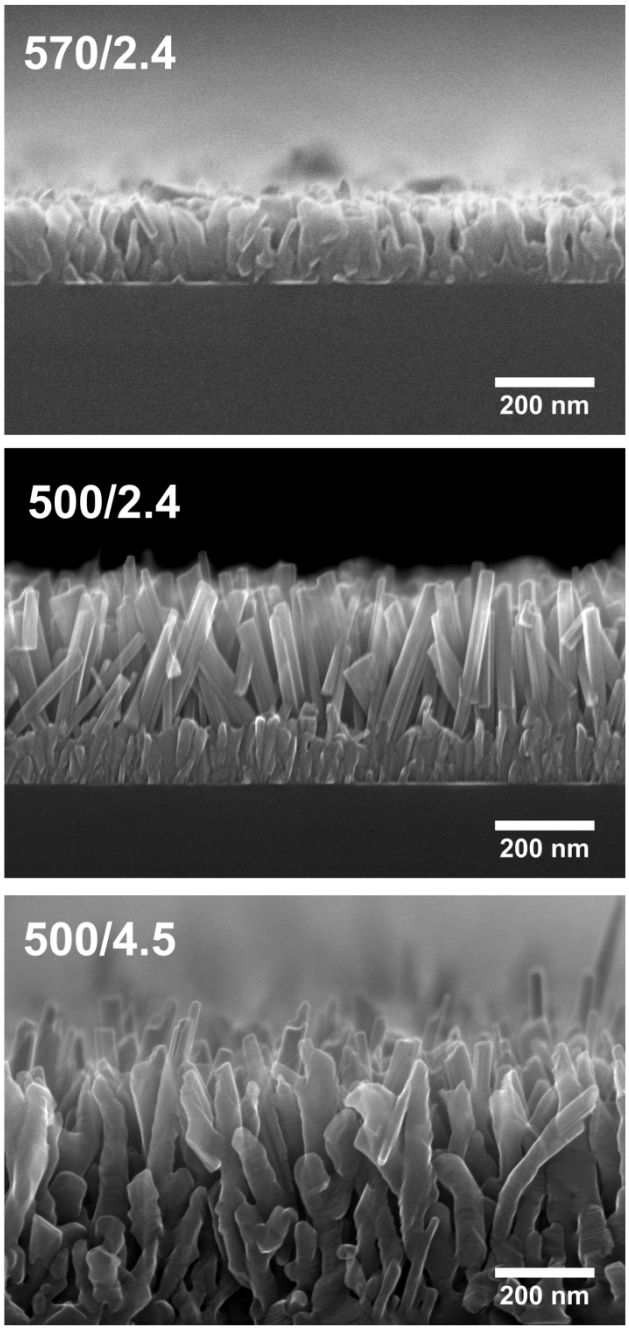

Figure 9 SEM micrographs of the molybdenum oxide film cross sections deposited at [T]/[P] of 570/2.4, 500/2.4 and 500/4.5.

mainly MoO_3 with some Mo_4O_{11}, which contains both Mo^{6+} and Mo^{5+} oxidation states. The proportions of cation oxidation states lead to an estimated film composition of 75 % MoO_3, 25 % Mo_4O_{11}. However, the Mo^{5+} could be partly due to surface reduction of MoO_3 or oxygen vacancies in the bulk, and the amorphous phase likely comprises both Mo^{5+} and Mo^{6+}. The 500/2.4 film has approximately equal proportions of Mo^{6+} and Mo^{5+}. This is in keeping with the distribution of Mo^{5+} and Mo^{6+} in Mo_4O_{11}. In addition, there is a small amount of Mo^{4+}. This gives an estimated film composition of 97 % Mo_4O_{11}, 3 % MoO_2, in agreement with the phases indicated by XRD. Yet, the XRD reflections of Mo_4O_{11} and MoO_2 are of the same order of magnitude, which suggests a higher content of MoO_2 than 3 %. This underestimation of Mo^{4+} is most likely due to the film morphology; assuming from SEM that MoO_2 is confined to the bottom of the film, it is beyond the sampling depth of XPS. For the 570/2.4 film, the Mo 3*d* spectrum shows a well-resolved, narrow peak at the binding energy of Mo^{4+} (229.82 eV). However, due to complications with the number of components in Mo 3*d*, including screened and unscreened peaks of the intrinsic Mo^{4+} spectrum, it is preferable to fit the components of the three oxidation states to the Mo 3*p* peaks.[52] The large Mo^{4+} content (39.5 %) shows that the film is mainly MoO_2. This Mo^{4+} content is likely even higher, due to atmospheric oxidation of the surface. This conclusion is consistent with the XRD result that showed that sample has mainly MoO_2 reflections. The remainder is equal amounts of Mo^{6+} and Mo^{5+}, which can be partly attributed to the Mo_4O_{11} content and partly related to surface oxides. Considering XPS alone gives a film composition of 60 % Mo_4O_{11}, 40 % MoO_2,

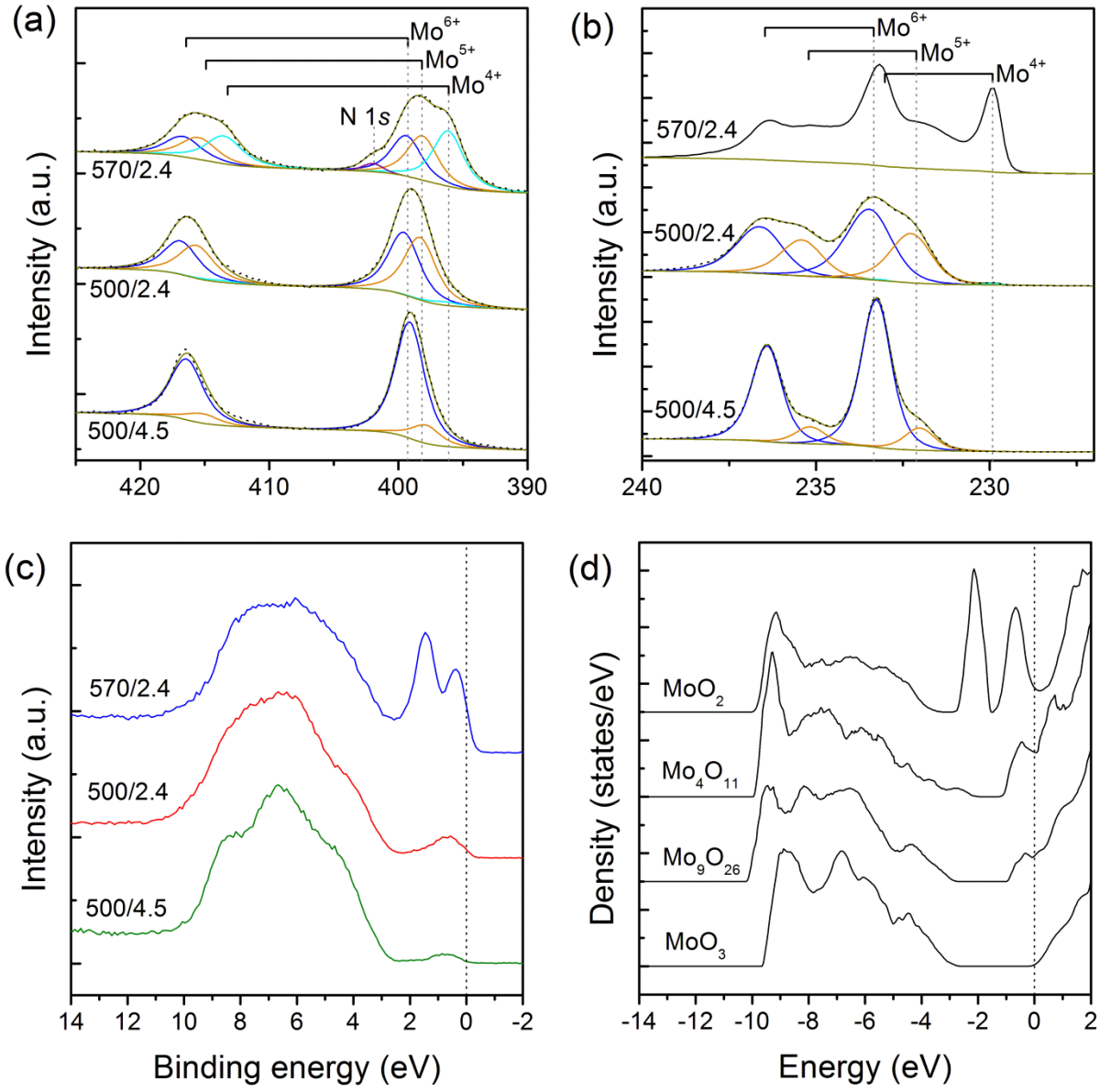

Figure 10 XPS spectra of the molybdenum oxide films, a) Mo 3*p* peaks; b) Mo 3*d* peaks; c) the valence band region. d) Calculated DOSes of molybdenum oxides weighted to the ionization cross-sections of Mo 4*d* and Mo O 2*p*. The DOS of MoO_3 is aligned to 0 eV at the CBM, and data has been smoothed by 15 point adjacent averaging.

but the XRD pattern indicates that the film is partially amorphous and shows only weak Mo_4O_{11} reflections. Thus, some of the Mo^{5+} and Mo^{6+} is likely to be contained in the amorphous phase. There is also small amount of nitrogen impurity incorporated in the 570/2.4 film, revealed in the N 1*s* peak in the Mo 3*p* spectra. Nitrogen impurities are thought to promote the formation of oxygen vacancies in MoO_3, and nitridation improves the electrical conductivity of both MoO_3 and MoO_2 by the formation of molybdenum oxynitrides and molybdenum nitride.[75–77]

The valence band spectra in Figure 10c have been calibrated to the Fermi level of a metal contact, determined by a step function. The Fermi level is aligned to 0 eV. In order to compare the spectra to the calculated DOSes, the intensities of the Mo 4*d* and O 2*p* partial DOSes are shown in Figure 10d weighted to the one-electron ionization cross-sections of 0.92 kb and 0.06 kb respectively.[52] The valence band region is made up of mainly O 2*p* states in the 10 – 3 eV range, and Mo 4*d* states adjacent to the Fermi level. The valence band has a similar energy range and width in the calculated DOS. There are prominent shoulders on the O 2*p* states of the 500/4.5 film, which reflects the anisotropy of Mo–O bonding of MoO_3 and can also be recognized in the MoO_3 weighted DOS.[78] The Mo 4*d* states are filled with progressing reduction, and show a broad signal at approximately 1 eV below the Fermi level for the 500/4.5 and 500/2.4 films. The 570/2.4 film exhibits two peaks below the Fermi energy that are distinctive of MoO_2. It is possible that there are other components contributing, as there is a continuum of states between the top of the valence band and the Mo 4*d* states which is not seen in the calculated DOS. This could be due to the amorphous content of the film. Despite the presence of Mo^{4+} in the 500/2.4 film, the gap states are broad, weak and without two distinct peaks. This can be related back to the microstructure of the films, where the phase segregation means that most of the MoO_2 content is not within the XPS sampling depth. At 0 eV, the 570/2.4 film has metallic behaviour, while the valence band maximum for the other two samples are slightly shifted with respect to the Fermi level. The 500/2.4 film is also showing metallic behaviour as some filled states coincide with the Fermi level position. For the 500/4.5 film, the signal is too weak to determine if there is a gap between the Fermi level and the gap states.

In comparison with the calculated DOS, the Mo 4*d* peaks of the 500/4.5 and 500/2.4 films could be attributed to either MoO_3 with oxygen vacancies, Mo_4O_{11}, or Mo_9O_{26}. Despite the low stability of the point defects compared to the reduced phases, there are likely point defects still present in the MoO_3 due to the role of kinetics and entropy contribution above 0 K. There is certainly a contribution from the Mo_4O_{11} phase, and despite the weak XPS signal at the Fermi level, from the calculated DOS we can expect metallic behaviour with Mo_4O_{11} being present. The possibility of Mo_9O_{26} being present can also be considered, as small quantities may not be detected by XRD. Because of the calculated stability of Mo_9O_{26} between MoO_3 and Mo_4O_{11}, the presence of the Mo_9O_{26} phase is not unlikely in the 500/4.5 film.

The 500/4.5 film has a transmittance of 50% in the visible range (Figure 11a). This is lower than the reported transmittance of MoO_3 films due to the Mo_4O_{11} content.[79] The optical band gap of the films, E_g, can be estimated by utilizing the relation, $(\alpha h\nu)^n = A(h\nu - E_g)$ where α is the absorption coefficient, *h* is the Planck constant, *ν* is the frequency of light and *A* is the band edge parameter. The Tauc plot of $(\alpha h\nu)^2$ versus photon energy $(h\nu)$ is shown in the inset in Figure 11.

Table 4 Spectral fitting of Mo 3*p* and Mo 3*d* peaks: Mo $3d_{5/2}$ and Mo $3p_{3/2}$ binding energy (eV), FWHM value (eV), and the relative content of 4+, 5+ and 6+ oxidation states of Mo (%). The distribution of oxidation states is found from deconvolution of both Mo $3d_{5/2}$ and Mo $3d_{3/2}$ for Mo 3*d*, and from both Mo $3p_{3/2}$ and Mo $3p_{1/2}$ for Mo 3*p*.

	Mo $3p_{3/2}$			Mo $3d_{5/2}$		
	Mo^{4+} BE (eV), FWHM (eV) Content (%)	Mo^{5+} BE (eV), FWHM (eV) Content (%)	Mo^{6+} BE (eV), FWHM (eV) Content (%)	Mo^{4+} BE (eV), FWHM (eV) Content (%)	Mo^{5+} BE (eV), FWHM (eV) Content (%)	Mo^{6+} BE (eV), FWHM (eV) Content (%)
500/4.5	0	397.87 2.68 13.6 %	399.12 2.68 86.4 %	0	232.01 1.01 13.8 %	233.25 1.01 86.2 %
500/2.4	396.31 2.90 2.7 %	398.31 2.90 48.5 %	399.56 2.90 48.8 %	229.82 0.36 0.5 %	232.22 1.36 39.4 %	233.42 1.51 60.1 %
570/2.4	396.13 2.78 39.5 %	398.13 2.78 31.6 %	399.38 2.78 28.9 %	-	-	-

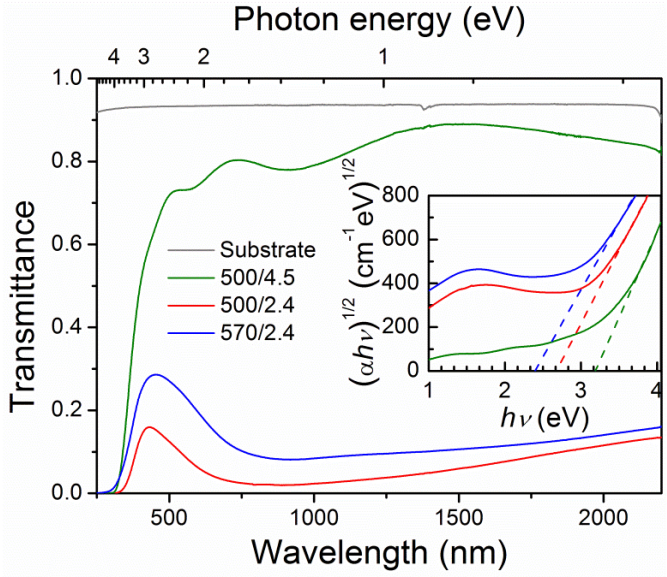

Figure 11 Transmittance spectra for the three molybdenum oxide films and the quartz substrate. Inset, the corresponding Tauc plot of $(\alpha h\nu)^{0.5}$ of the samples, for indirect transitions.

The exponent *n* is set as 0.5 for allowed indirect transitions. α is defined by transmittance $T = e^{-\alpha z}$ where *z* is the optical path length which is taken as the film thickness. Direct transitions (n = 2) are often used to describe crystalline MoO_3 films, with reported optical band gaps in the range 2.8 to 3.5 eV.[17,23,79–81] However, When allowed direct transitions are plotted for amorphous films, a larger band gap is generally predicted, up to 4 eV, due to the wider absorption edge.[79,82] Instead, when indirect transitions are considered for amorphous MoO_3 films band gaps of 2.7 to 3.5 eV are estimated.[6,32,34,83] Indirect transitions are commonly used for amorphous materials, such as in the initial development of the model by Tauc *et al.*[84] Relating this to the thin films of MoO_3 characterized here, it follows that n = ½ is appropriate for these films which are not completely crystalline, and indeed this gives a better approximation to linear behaviour. Plotting this, the linear region of the 500/2.4 film is extrapolated to give a band gap 3.2 eV, which matches with reports for MoO_3 thin films.[11,53] The more reduced films have a drastically reduced transmittance compared to the 500/4.5 (Figure 11). As the more reduced films are thinner, this lower transmittance is directly related to the change in composition. The difference between the transmittance of the 500/2.4 and 570/2.4 films, however, can be related to the change in film thickness. The optical band gaps of the 500/2.4 and 570/2.4 films are also lower at 2.7 eV and 2.4 eV respectively. This and the wider absorption edge are a result of the higher proportion of reduced phases due to the position of their absorption bands, for example Mo_4O_{11} (1.3 eV, 2.13 eV and 2.42 eV) and Mo_9O_{26} (2.12 eV), or MoO_2 (2.48 eV).[85]

Conclusions

The crystal structures, electronic structures and electrical and optical properties of molybdenum oxide thin films were investigated with change in O/Mo ratio. Modelling of oxygen vacancy concentrations in MoO_3 showed that the cost of removing the oxygen pointing towards the van der Waals gap is lowest. Modelling of the possible structures in the stoichiometry range MoO_2 to MoO_3 has shown that the layered van der Waals structure $Mo_{18}O_{52}$ is destabilized by loss of oxygen from the lattice, and enables restructuring to the ReO_3 based structure Mo_9O_{26}. Furthermore, point defects are less energetically favourable than shear structures at all vacancy concentrations investigated. Density of states calculations showed a similar metallic DOS for Mo_4O_{11} and Mo_9O_{26} phases, compared to the distinctive two peaks of the MoO_2 DOS, and the wide gap MoO_3. The metallic DOSes differed from the gap states modelled for point defects in MoO_3. In synthesised films, MoO_2, Mo_4O_{11} and MoO_3 phases were detected in varying ratios in three films. The phase composition affected the electronic and optical properties, with Mo_4O_{11} and MoO_2 content lowering the resistivity, transmittance and band gap. The valence band region measured by XPS was compared to the calculated DOS; MoO_2 could be discerned by its two peaks, whereas Mo_4O_{11}, Mo_9O_{26} and oxygen vacancies in MoO_3 could all contribute to the peak from 0 to 2 eV.

Acknowledgements

This work was performed within The Norwegian Research Centre for Solar Cell Technology project number 193829, a Centre for Environmentally-friendly Energy Research co-sponsored by the Norwegian Research Council and research and industry partners in Norway. Computational resources were provided by NOTUR, The Norwegian Metacentre for Computational Science, through the project nn9264k. NTNU NanoLab is acknowledged for support and subsidized use of their facilities.

References

1 Wang, P.-S.; Lo, Y.-Y.; Tseng, W.-H.; Chen, M.-H.; Wu, C.-I. Enhancing the Incorporation Compatibility of Molybdenum Oxides in Organic Light Emitting Diodes with Gap State Formations. *J. Appl. Phys.* **2013**, *114* (6), 63710.

2 Liang, J.; Zu, F.-S.; Ding, L.; Xu, M.-F.; Shi, X.-B.; Wang, Z.-K.; Liao, L.-S. Aqueous Solution-Processed MoO_3 Thick Films as Hole Injection and Short-Circuit Barrier Layer in Large-Area Organic Light-Emitting Devices. *Appl. Phys. Express* **2014**, *7*, 111601.

3 Xiang, D.; Han, C.; Zhang, J.; Chen, W. Gap States Assisted MoO_3 Nanobelt Photodetector with Wide Spectrum Response. *Sci. Rep.* **2014**, *4*, 4891.

4 Alsaif, M. M. Y. A.; Field, M. R.; Murdoch, B. J.; Daeneke, T.; Latham, K.; Chrimes, A. F.; Zoolfakar, A. S.; Russo, S. P.; Ou, J. Z.; Kalantar-zadeh, K. Substoichiometric Two-Dimensional Molybdenum Oxide Flakes: A Plasmonic Gas Sensing Platform. *Nanoscale* **2014**, *6*, 12780–12791.

5 Bai, S.; Chen, S.; Chen, L.; Zhang, K.; Luo, R.; Li, D.; Liu, C. C. Ultrasonic Synthesis of MoO_3 Nanorods and Their Gas Sensing Properties. *Sensors Actuators, B Chem.* **2012**, *174* (2), 51–58.

6 Dasgupta, B.; Ren, Y.; Wong, L. M.; Kong, L.; Tok, E. S.; Chim, W. K.; Chiam, S. Y. Detrimental Effects of Oxygen Vacancies in Electrochromic Molybdenum Oxide. *J. Phys. Chem. C* **2015**, *119* (19), 10592–10601.

7 Yoosuf Ameen, M.; Pradhan, S.; Remyth Suresh, M.; Reddy, V. S. MoO_3 Anode Buffer Layer for Efficient and Stable Small Molecular Organic Solar Cells. *Opt. Mater. (Amst).* **2015**, *39*, 134–139.

8 Baldoni, M.; Craco, L.; Seifert, G.; Leoni, S. A Two-Electron Mechanism of Lithium Insertion into Layered α-MoO_3: A DFT and DFT+U Study. *J. Mater. Chem. A* **2013**, *1* (5), 1778.

9 Majhi, K.; Bertoluzzi, L.; Rietwyk, K. J.; Ginsburg, A.; Keller, D. A.; Lopez-Varo, P.; Anderson, A. Y.; Bisquert, J.; Zaban, A. Combinatorial Investigation and Modelling of MoO_3 Hole-Selective Contact in $TiO_2|Co_3O_4|MoO_3$ All-Oxide Solar Cells. *Adv. Mater. Interfaces* **2016**, *3*, 1500405.

10 Alsaif, M. M. Y. A.; Latham, K.; Field, M. R.; Yao, D. D.; Medehkar, N. V.; Beane, G. A.; Kaner, R. B.; Russo, S. P.; Ou, J. Z.; Kalantar-zadeh, K. Tunable Plasmon Resonances in Two-Dimensional Molybdenum Oxide Nanoflakes. *Adv. Mater.* **2014**, *26* (23), 3931–3937.

11 Balendhran, S.; Deng, J.; Ou, J. Z.; Walia, S.; Scott, J.; Tang, J.; Wang, K. L.; Field, M. R.; Russo, S.; Zhuiykov, S.; Strano, M. S.; Medhekar, N.; Sriram, S.; Bhaskaran, M.; Kalantar-zadeh, K. Enhanced Charge Carrier Mobility in Two-Dimensional High Dielectric Molybdenum Oxide. *Adv. Mater.* **2013**, *25*, 109–114.

12 Hanlon, D.; Backes, C.; Higgins, T. M.; Hughes, M.; O'Neill, A.; King, P.; McEvoy, N.; Duesberg, G. S.; Mendoza Sanchez, B.; Pettersson, H.; Nicolosi, V.; Coleman, J. N. Production of Molybdenum Trioxide Nanosheets by Liquid Exfoliation and Their Application in High-Performance Supercapacitors. *Chem. Mater.* **2014**, *26*, 1751–1763.

13 Lupan, O.; Trofim, V.; Cretu, V.; Stamov, I.; Syrbu, N. N.; Tiginyanu, I.; Mishra, Y. K.; Adelung, R. Investigation of Optical Properties and Electronic Transitions in Bulk and Nano-Microribbons of Molybdenum Trioxide. *J. Phys. D. Appl. Phys.* **2014**, *47* (8), 85302.

14 Shen, Y.; Deng, S.; Zhang, Y.; Liu, F.; Chen, J.; Xu, N. Highly Conductive Vertically Aligned Molybdenum Nanowalls and Their Field Emission Property. *Nanoscale Res. Lett.* **2012**, *7* (1), 463.

15 Sinaim, H.; Ham, D. J.; Lee, J. S.; Phuruangrat, A.; Thongtem, S.; Thongtem, T. Free-Polymer Controlling Morphology of α-MoO_3 Nanobelts by a Facile Hydrothermal Synthesis, Their Electrochemistry for Hydrogen Evolution Reactions and Optical Properties. *J. Alloys Compd.* **2012**, *516*, 172–178.

16 Shafiei, M.; Yu, J.; Breedon, M.; Motta, N.; Wu, Q.; Hu, Z.; Qian, L.; Kalantar-zadeh, K.; Wlodarski, W. Hydrogen Gas Sensors Based On Thermally Evaporated Nanostructured MoO_3 Schottky Diode: A Comparative Study. *IEEE Sensors* **2011**, 8–11.

17 Illyaskutty, N.; Sreedhar, S.; Sanal Kumar, G.; Kohler, H.; Schwotzer, M.; Natzeck, C.; Pillai, V. P. M. Alteration of Architecture of MoO_3 Nanostructures on Arbitrary Substrates: Growth Kinetics, Spectroscopic and Gas Sensing Properties. *Nanoscale* **2014**, *6* (22), 13882–13894.

18 Navas, I.; Vinodkumar, R.; Mahadevan Pillai, V. P. Self-Assembly and Photoluminescence of Molybdenum Oxide Nanoparticles. *Appl. Phys. A* **2011**, *103* (2), 373–380.

19 Brezesinski, T.; Wang, J.; Tolbert, S. H.; Dunn, B. Ordered Mesoporous α-MoO_3 with Iso-Oriented Nanocrystalline Walls for Thin-Film Pseudocapacitors. *Nat. Mater.* **2010**, *9* (2), 146–151.

20 Lee, Y. J.; Park, C. W.; Kim, D.; Nichols, W. T.; Oh, S.; Kim, Y. Do. MoO_3 Thin Film Synthesis by Chemical Vapor Transport of Volatile $MoO_3(OH)_2$. *J. Ceram. Process. Res.* **2010**, *11* (1), 52–55.

21 Gavrilyuk, A.; Tritthart, U.; Gey, W. The Nature of the Photochromism Arising in the Nanosized MoO_3 Films. *Sol. Energy Mater. Sol. Cells* **2011**, *95* (7), 1846–1851.

22 Hsu, C.-S.; Chan, C.-C.; Huang, H.-T.; Peng, C.-H.; Hsu, W.-C. Electrochromic Properties of Nanocrystalline MoO_3 Thin Films. *Thin Solid Films* **2008**, *516* (15), 4839–4844.

23 Yang, W.-Q.; Wei, Z.-R.; Zhu, X.-H.; Yang, D.-Y. Strong Influence of Substrate Temperature on the Growth of Nanocrystalline MoO_3 Thin Films. *Phys. Lett. A* **2009**, *373* (43), 3965–3968.

24 Jiebing, S.; Rui, X.; Shimin, W.; Wufeng, T.; Hua, T.; Jing, S. Preparation and Characterization of Molybdenum Oxide Thin Films by Sol-Gel Process. *J. Sol-Gel Sci. Technol.* **2003**, *27* (3), 315–319.

25 Rouhani, M.; Foo, Y. L.; Hobley, J.; Pan, J.; Subramanian, G. S.; Yu, X.; Rusydi, A.; Gorelik, S. Photochromism of Amorphous Molybdenum Oxide Films with Different Initial Mo^{5+} Relative Concentrations. *Appl. Surf. Sci.* **2013**, *273*, 150–158.

26 Haitao, X.; Xiang, Z. Investigation of Hole Injection Enhancement by MoO_3 Buffer Layer in Organic Light Emitting Diodes. *J. Appl. Phys.* **2013**, *114* (24), 244505.

27 Shi, X.-B.; Xu, M.-F.; Zhou, D.-Y.; Wang, Z.-K.; Liao, L.-S. Improved Cation Valence State in Molybdenum Oxides by Ultraviolet-Ozone Treatments and Its Applications in Organic Light-Emitting Diodes. *Appl. Phys. Lett.* **2013**, *102*, 233304.

28 Smith, G. B.; Golestan, D.; Gentle, A. R. The Insulator to Correlated Metal Phase Transition in Molybdenum Oxides. *Appl. Phys. Lett.* **2013**, *103* (5), 51119.

29 Yao, D. D.; Ou, J. Z.; Latham, K.; Zhuiykov, S.; O'Mullane, A. P.; Kalantar-zadeh, K. Electrodeposited α- and SS-Phase MoO_3 Films and Investigation of Their Gasochromic Propertie. *Cryst. Growth Des.* **2012**, *12*, 1865–1870.

30 Ohtsuka, H.; Sakurai, Y. Characterization of MoO_{3-X} Thin Films. *Jpn. J. Appl. Phys.* **2001**, *40* (1), 4680–4683.

31 Simchi, H.; McCandless, B. E.; Meng, T.; Boyle, J. H.; Shafarman, W. N. Characterization of Reactively Sputtered Molybdenum Oxide Films for Solar Cell Application. *J. Appl. Phys.* **2013**, *114*, 13503.

32 Bica De Moraes, M. A.; Trasferetti, B. C.; Rouxinol, F. P.; Landers, R.; Durrant, S. F.; Scarmínio, J.; Urbano, A. Molybdenum Oxide Thin Films Obtained by the Hot-Filament Metal Oxide Deposition Technique. *Chem. Mater.* **2004**, *16* (3), 513–520.

33 Jasieniak, J. J.; Seifter, J.; Jo, J.; Mates, T.; Heeger, A. J. A Solution-Processed MoO_x Anode Interlayer for Use within Organic Photovoltaic Devices. *Adv. Funct. Mater.* **2012**, *22*, 2594–2605.

34 Gretener, C.; Perrenoud, J.; Kranz, L.; Baechler, C.; Yoon, S.; Romanyuk, Y. E.; Buecheler, S.; Tiwari, A. N. Development of MoO_x Thin Films as Back Contact Buffer for CdTe Solar Cells in Substrate Configuration. *Thin Solid Films* **2013**, *535*, 193–197.

35 Fu, Q.; Chen, J.; Shi, C.; Ma, D. Room-Temperature Sol-Gel Derived Molybdenum Oxide Thin Films for Efficient and Stable Solution-Processed Organic Light-Emitting Diodes. *ACS Appl. Mater. Interfaces* **2013**, *5* (13), 6024–6029.

36 Meyer, J.; Kidambi, P. R.; Bayer, B. C.; Weijtens, C.; Kuhn, A.; Centeno, A.; Pesquera, A.; Zurutuza, A.; Robertson, J.; Hofmann, S. Metal Oxide Induced Charge Transfer Doping and Band Alignment of Graphene Electrodes for Efficient Organic Light Emitting Diodes. *Sci. Rep.* **2014**, *4*, 5380.

37 Battaglia, C.; Yin, X.; Zheng, M.; Sharp, I. D.; Chen, T.; McDonnell, S.; Azcatl, A.; Carraro, C.; Ma, B.; Maboudian, R.; Wallace, R. M.; Javey, A. Hole Selective MoO_x Contact for Silicon Solar Cells. *NanoLetters* **2014**, *14*, 967–971.

38 Kim, H.-S.; Cook, J. B.; Lin, H.; Ko, J. S.; Tolbert, S. H.; Ozolins, V.; Dunn, B. Oxygen Vacancies Enhance Pseudocapacitive

Charge Storage Properties of MoO_{3-x}. *Nat. Mater.* **2016**, doi:10.1038/nmat4810.
39 Gai-Boyes, P. L. Defects in Oxide Catalysts: Fundamental Studies of Catalysis in Action. *Catal. Rev.* **1992**, *34*, 1–54.
40 Smith, R. L.; Rohrer, G. S. Scanning Probe Microscopy of Cleaved Molybdates: α-MoO_3(010), $Mo_{18}O_{52}$(100), Mo_8O_{23}(010), and η-Mo_4O_{11}(100). *J. Solid State Chem.* **1996**, *124* (124), 104–115.
41 Gai, P. L.; Boyes, E. D. Electron Microscopy Studies of Catalysis by Oxides. In *Electron Microscopy in Heterogeneous Catalysis*; Institute of Physics Publishing: Bristol and Philidelphia, 2003; pp 89–140.
42 Bursill, L. A. Electron Microscope Study of an Homologous Series of Shear Structures Based on Molybdenum Trioxide. *Acta Crystallogr.* **1972**, *A28* (2), 187–191.
43 Floquet, N.; Bertrand, O. Reactivity of the $Mo_{18}O_{52}$ (100) Surface: A Study by RHEED of the $Mo_{18}O_{52}$-MoO_3 Structural Transformation. *Solid State Ionics* **1989**, *32/33*, 234–243.
44 Kihlborg, L. The Crystal Structure of $Mo_{18}O_{52}$ and the Existence of Homologous Series of Structures Based on MoO_3. *Ark. för Kemi* **1963**, *21*, 443–460.
45 Magnéli, A. The Crystal Structures of Mo_9O_{26} (ß'-Molybdenum Oxide) and Mo_8O_{23} (SS-Molybdenum Oxid). *Acta Chemica Scandinavica*. 1948, pp 501–517.
46 Sato, M.; Onoda, O.; Matsuda, Y. Structural Transitions in Mo_nO_{3n-1} (n=9 and 10). *J.Phys. C Solid State Phys.* **1987**, *20*, 4763–4771.
47 Brocławik, E.; Haber, J. SCF-SW-Xα Calculations of the Removal of Oxygen from Oxide Surfaces by Vacancy Formation and Crystallographic Shear Mechanisms. *J. Catal.* **1981**, *72*, 379–382.
48 Kihlborg, L. The Crystal Structure of $Mo_{17}O_{47}$. *Acta Chemica Scandinavica*. 1960, pp 1612–1622.
49 Bursill, L. A. On the Relation Between Molybdenum Trioxide and Rhenium Trioxide Type Crystal Structures. *Acta Crystallogr.* **1973**, *A29* (1), 28–30.
50 Åsbrink, S.; Kihlborg, L. A Study of the Crystal Symmetry and Structure of Orthorhombic Mo_4O_{11} by Least-Squares Techniques. *Acta Chem. Scand.* **1964**, *18* (6), 1571–1573.
51 Zhang, C.; Gao, M. C.; Yang, Y.; Zhang, F. Thermodynamic Modeling and First-Principles Calculations of the Mo-O System. *Calphad Comput. Coupling Phase Diagrams Thermochem.* **2014**, *45*, 178–187.
52 Scanlon, D. O.; Watson, G. W.; Payne, D. J.; Atkinson, G. R.; Egdell, R. G.; Law, D. S. L. Theoretical and Experimental Study of the Electronic Structures of MoO_3 and MoO_2. *J. Phys. Chem. C* **2010**, *114*, 4636–4645.
53 Carcia, P. F.; McCarron III, E. M. Synthesis and Properties of Thin Film Polymorphs of Molybdenum Trioxide. *Thin Solid Films* **1987**, *155*, 53–63.
54 Tokarz-Sobieraj, R.; Hermann, K.; Witko, M.; Blume, A.; Mestl, G.; Schlögl, R. Properties of Oxygen Sites at the MoO_3(010) Surface: Density Functional Theory Cluster Studies and Photoemission Experiments. *Surf. Sci.* **2001**, *489* (1–3), 107–125.
55 Coquet, R.; Willock, D. J. The (010) Surface of α-MoO_3, a DFT + U Study. *Phys. Chem. Chem. Phys.* **2005**, *7*, 3819–3828.
56 Greiner, M. T.; Chai, L.; Helander, M. G.; Tang, W. M.; Lu, Z. H. Metal/Metal-Oxide Interfaces: How Metal Contacts Affect the Work Function and Band Structure of MoO_3. *Adv. Funct. Mater.* **2013**, *23*, 215–226.
57 Huang, P.-R.; He, Y.; Cao, C.; Lu, Z.-H. Impact of Lattice Distortion and Electron Doping on α-MoO_3 Electronic Structure. *Sci. Rep.* **2014**, *4*, 7131.
58 Goodenough, J. B. Metallic Oxides. *Prog. Solid State Chem.* **1971**, *5* (C), 145–399.
59 Kresse, G.; Hafner, J. Ab Initio Molecular Dynamics for Liquid Metals. *Phys. Rev. B* **1993**, *47*, 558–561.
60 Kresse, G.; Furthmüller, J. Efficiency of Ab Initio Total Energy Calculations for Metals and Semiconductors Using a Plane-Wave Basis Set. *Comput. Mater. Sci.* **1996**, *6*, 15–50.
61 Kresse, G.; Furthmüller, J. Efficient Iterative Schemes for Ab Initio Total-Energy Calculations Using a Plane-Wave Basis Set. *Phys. Rev. B* **1996**, *54*, 11169–11186.
62 Kresse, G.; Joubert, D. From Ultrasoft Pseudopotentials to the Projector Augmented-Wave Method. *Phys. Rev. B* **1999**, *59*, 1758–1775.
63 Inzani, K.; Grande, T.; Vullum-Bruer, F.; Selbach, S. M. A van Der Waals Density Functional Study of MoO_3 and Its Oxygen Vacancies. *J. Phys. Chem. C* **2016**, *120* (16), 8959–8968.
64 Dudarev, S. L.; Botton, G. A.; Savrasov, S. Y.; Humphreys, C. J.; Sutton, A. P. Electron-Energy-Loss Spectra and the Structural Stability of Nickel Oxide: An LSDA+U Study. *Phys. Rev. B* **1998**, *57*, 1505–1509.
65 Schimka, L.; Harl, J.; Kresse, G. Improved Hybrid Functional for Solids: The HSEsol Functional. *J. Chem. Phys.* **2011**, *134* (2), 24116.
66 Manivannan, V.; Tichy, R.; Goodenough, J. B. Synthesis and Characterization of Reduced Molybdenum Oxides with Hydroxylamine Hydrochloride in Aqueous Solutions. *J. Solid State Chem.* **1999**, *273*, 269–273.
67 Kihlborg, L. Least Squares Refinement of the Crystal Structure of Molybdenum Trioxide. *Ark. för Kemi* **1963**, *21*, 357–364.
68 Baur, W. H. The Geometry of Polyhedral Distortions. Predictive Relationships for the Phosphate Group. *Acta Crystallogr. Sect. B Struct. Crystallogr. Cryst. Chem.* **1974**, *30* (5), 1195–1215.
69 Kihlborg, L. Studies on Molybdenum Oxides. *Acta Chemica Scandinavica*. 1959, pp 954–962.
70 Hautier, G. Data Mining Approaches to High-Throughput Crystal Structure and Compound Prediction. In *Prediction and Calculation of Crystal Structures: Methods and Applications*; Atahan-Evrenk, Ş., Aspuru-Guzik, A., Eds.; Springer, 2014; pp 139–180.
71 Brewer, L.; Lamoreaux, R. H. The Mo-O System (Molybdenum-Oxygen). *Bull. Alloy Phase Diagrams* **1980**, *1* (2), 85–89.
72 Bursill, L. A. Crystallographic Shear in Molybdenum Trioxide. *Proc. R. Soc. Lond. A. Math. Phys. Sci.* **1969**, *311*, 267–290.
73 McCarron III, E. M. SS-MoO_3: A Metastable Analogue of WO₃. *J. Chem. Soc. Chem. Commun.* **1986**, No. 4, 336–338.
74 Rogers, D. B.; Shannon, R. D.; Sleight, A. W.; Gillson, J. L. Crystal Chemistry of Metal Dioxides with Rutile-Related Structures. *Inorg. Chem.* **1969**, *8* (4), 841–849.
75 Labanowska, M. Paramagnetic Defects in MoO_3-Revisited. *Phys. Chem. Chem. Phys.* **1999**, *1*, 5385–5392.
76 Ji, W.; Shen, R.; Yang, R.; Yu, G.; Guo, X.; Peng, L.; Ding, W. Partially Nitrided Molybdenum Trioxide with Promoted Performance as an Anode Material for Lithium-Ion Batteries. *J. Mater. Chem. A* **2014**, *2* (3), 699–704.
77 Yoon, S.; Jung, K. N.; Jin, C. S.; Shin, K. H. Synthesis of Nitrided MoO_2 and Its Application as Anode Materials for Lithium-Ion Batteries. *J. Alloys Compd.* **2012**, *536*, 179–183.
78 Sato, H.; Mukaegawa, Y.; Maso, H.; Utsumi, Y.; Tezuka, Y.; Morimoto, O.; Negishi, H.; Negishi, S.; Namatame, H.; Taniguchi, M. Soft X-Ray Absorption and Emission Study on Anisotropic Electronic Structure of MoO_3. *J. Electron Spectros. Relat. Phenomena* **2010**, *181* (2–3), 211–214.
79 Buono-Core, G. E.; Cabello, G.; Klahn, A. H.; Lucero, A.; Nuñez, M. V; Torrejón, B.; Castillo, C. Growth and Characterization of Molybdenum Oxide Thin Films Prepared by Photochemical Metal-Organic Deposition (PMOD). *Polyhedron* **2010**, *29* (6), 1551–1554.

80 Vasilopoulou, M.; Douvas, A. M.; Georgiadou, D. G.; Palilis, L. C.; Kennou, S.; Sygellou, L.; Soultati, A.; Kostis, I.; Papadimitropoulos, G.; Davazoglou, D.; Argitis, P. The Influence of Hydrogenation and Oxygen Vacancies on Molybdenum Oxides Work Function and Gap States for Application in Organic Optoelectronics. *J. Am. Chem. Soc.* **2012**, *134* (39), 16178–16187.
81 Sian, T. S.; Reddy, G. B. Optical, Structural and Photoelectron Spectroscopic Studies on Amorphous and Crystalline Molybdenum Oxide Thin Films. *Sol. Energy Mater. Sol. Cells* **2004**, *82* (3), 375–386.
82 Lin, S.-Y.; Chen, Y.-C.; Wang, C.-M.; Hsieh, P.-T.; Shih, S.-C. Post-Annealing Effect upon Optical Properties of Electron Beam Evaporated Molybdenum Oxide Thin Films. *Appl. Surf. Sci.* **2009**, *255* (6), 3868–3874.
83 He, T.; Yao, J. Photochromism of Molybdenum Oxide. *J. Photochem. Photobiol. C Photochem. Rev.* **2003**, *4* (2), 125–143.
84 Tauc, J.; Grigorovici, R.; Vancu, A. Optical Properties and Electronic Structure of Amorphous Geranium. *Phys. Status Solidi* **1966**, *15*, 627–637.
85 Porter, V. R.; White, W. B.; Roy, R. Optical Spectra of the Intermediate Oxides of Titanium, Vanadium, Molybdenum, and Tungsten. *J. Solid State Chem.* **1972**, *4*, 250–254.

